Wall pressure spectra on a DU96-W-180 profile from low to pre-stall angles of attack

Alexandre Suryadi*† and Michaela Herr*‡

German Aerospace Center (DLR), D-38108 Braunschweig, Germany

In an effort to characterize noise induced by separated turbulent boundary layers, surface pressure fluctuations on a DU96-W-180 airfoil were measured using miniature pressure sensors. Because of limitation in amplifier channels and available sensors, a rearrangeable configuration of sensors was applied. Chordwise distributions of the surface pressure were obtained for aerodynamic angles of attack of $-0.8^\circ \leq \alpha \leq 10.3^\circ$ and at three Reynolds numbers (0.8, 1.0, and 1.2) $\times 10^6$. The boundary layer profile at 1%c behind the trailing edge was measured using constant temperature anemometry. The boundary layer thickness compares well with that simulated using XFOIL for $\alpha \leq 7.8^\circ$. Within the limits of the simulation, other relevant boundary layer properties from XFOIL were used to calculate the surface pressure spectrum predicted from published empirical models for zero and non-zero pressure gradient turbulent boundary layers. Finally, a modified Blake-TNO semi-empirical model was used to predict the surface pressure spectrum near the trailing edge for separated flow. The modification is introduced to the so called 'moving axis spectrum' and the chord-normal correlation length scale. It is found that in the low frequency range, the modified semi-empirical model fits well with the measured surface pressure spectrum of a separated turbulent boundary layer.

Nomenclature

a	Speed of sound, m·s^{-1}
c	Chord length, m
c_l	Coefficient of lift, -
c_1, c_2	Modification parameters to Φ_m, -
k_e	Eddy containing wavenumber, $0.7468/L_y$, m^{-1}
k_x	Chordwise wavenumber, $2\pi/L_x$, rad·m^{-1}
k_z	Spanwise wavenumber, $2\pi/L_z$, rad·m^{-1}
L	Wetted span, m
ℓ_{mix}	Mixing length, $0.085\delta \tanh(\kappa y/0.085\delta)$, m
L_x	Chordwise correlation length scale, m
L_y	Chord-normal correlation length scale, m
L_z	Spanwise correlation length scale, m
R	Radial distance from a sound source, m
Re	Reynolds number, -
R_T	Ratio of the outer and inner boundary layer time scales, $u_\tau \delta/\nu\sqrt{C_f/2}$
$U(y)$	Time averaged velocity component, m·s^{-1}
U_∞	Freestream velocity, m·s^{-1}
$U_c(y)$	Convective velocity, m·s^{-1}
U_e	Turbulent boundary layer edge velocity, m·s^{-1}
u, v, w	Instantaneous velocity components in the order x, y, z, m·s^{-1}

*Research Engineer, Institute of Aerodynamics and Flow Technology, Technical Acoustics; Lilienthalplatz 7, 38108 Braunschweig;

†alexandre.suryadi@dlr.de

‡michaela.herr@dlr.de

u', v', w'	Fluctuating velocity components in the order x, y, z, m·s^{-1}
u_τ	Friction velocity, m·s^{-1}
$S(\omega)$	Far-field noise power spectral density, Pa^2·s
x, y, z	Chordwise, chord-normal, and spanwise spatial directions
α	Aerodynamic angle of attack, $^\circ$
β_c	Clauser parameter, $\theta/\tau_w \mathrm{d}P/\mathrm{d}x$, -
δ	Boundary layer thickness, m
δ^*	Boundary layer displacement thickness, m
θ	Boundary layer momentum thickness, m
κ	von Kármán constant, 0.41
ν	Kinematic viscosity, m^2·s^{-1}
ρ	Density, kg·m^{-3}
Φ_m	Moving axis spectrum, s
Φ_{pp}	Surface pressure power spectral density, Pa^2·s
Φ_{vv}	Vertical velocity wavenumber power spectral density, -
τ_w	Wall shear stress, Pa
$\tau_{\max}$	Maximum shear stress, Pa
ω	Angular frequency, $2\pi f$, rad·s^{-1}

Abbreviations

APG	Adverse Pressure Gradient
AWB	Acoustic Wind Tunnel Braunschweig
CFAS	Catlett, Forest, Anderson, and Stewart[5]
LWT	Laminar Wind Tunnel
RRM	Rozenberg, Robert, and Moreau[11]
SR	Schüle and Rossignol[14]
ZPG	Zero Pressure Gradient

I. Introduction

Wind turbines in Germany are located near residential areas. To limit the acoustic effect of wind turbine installations to nearby populations, noise compliances are followed strictly. Because of atmospheric gust, the effective angle of attack of a wind turbine blade section can increase. Above a critical angle the boundary layer separates and it provide an additional component to the far-field noise. The mechanism of the generation of trailing edge noise and its prediction under attached boundary layer condition has been studied well.[3,4,9] An effort to improve the prediction of far-field noise for separated flow was reported in Schüle and Rossignol[14] by modifying the modeled surface pressure power spectral density that was described in Parchen.[10] While the result looks promising there is a lack of validation data on the behavior of the model at low frequency, mainly due to the limited resolution of available acoustic measurements techniques, such as elliptical-mirror directional microphone or microphone array systems. To bridge this gap, the surface pressure fluctuations were measured using miniature pressure sensors from Kulite semiconductors. Spanwise and chordwise distributions of surface pressure fluctuations were obtained for aerodynamic angles of attack $-0.8^\circ \leq \alpha \leq 10.3^\circ$ and at three Reynolds numbers Re=(0.8, 1.0, and 1.2) $\times 10^6$ in the Acoustic Wind Tunnel Braunschweig (AWB).

Under the assumptions that the flow is incompressible, the noise is solely produced by hydrodynamic surface pressure fluctuations, and the surface pressure from two sides contribute to the total far-field noise independently. The far-field noise on each side, $S(\omega)$, can be expressed as[3]

$$S(\omega) = \frac{1}{4\pi R^2}\left(\frac{\omega L}{a}\right)\int_{-\infty}^{\infty}\frac{\Phi_{pp}(k_x, 0, \omega)}{|k_x|[1-\omega/(ak_x)]}\,\mathrm{d}k_x \tag{1}$$

where R is the radial distance of the source to the observer, L is the wetted span, Φ_{pp} is the surface pressure spectrum, a is the speed of sound at sea level, ω is the angular frequency, and k_x is the chordwise wavenumber. The surface pressure power spectral density $\Phi_{pp}(k_x, k_y, \omega)$ can be modeled in terms of the air density ρ, the mean shear $\mathrm{d}U/\mathrm{d}y$, the correlation length scale L_y, the turbulent stress $\overline{v'v'}$, the turbulent spectra Φ_{vv}, and a modeled eddy decay spectrum, named 'moving axis spectrum' Φ_m that depends on the local convective

velocity U_c. These terms are integrated over the boundary layer height δ[2,10]

$$\begin{aligned}\Phi_{pp}(k_x,k_z,\omega) &= 4\rho^2\frac{k_x^2}{k_x^2+k_z^2}\int_0^\delta L_y(y)\left[\frac{\partial U}{\partial y}(y)\right]^2\overline{v'v'}(y)\Phi_{vv}(k_x,k_z,y)\\ &\quad \Phi_m[\omega-U_c(y)k_x]\exp[-2\sqrt{k_x^2+k_z^2}\,y]\,\mathrm{d}y \end{aligned} \tag{2}$$

where L_y and U_c were modeled in Schüle and Rossignol[14] to fit the far field noise affected by flow separation. The power spectral density $\Phi_{pp}(k_x,k_z,\omega)$ is assumed to be separable and has the following form[6]

$$\Phi_{pp}(k_x,k_z,\omega)=\Phi_{pp}(\omega)\Phi_{pp}(k_x)\Phi_{pp}(k_z) \tag{3}$$

The first term in the right hand side of Eq. (3) is the surface pressure autospectrum and the two other terms describe the convection and decay of turbulent eddies in their respective directions.

Three empirical models of the surface pressure autospectrum were developed by Goody,[8] Rozenberg et al.[11] and Catlett et al.[5] and they have the general form given as

$$\frac{\Phi_{pp}U_e}{\tau_w^2\delta}=\frac{a_1(\omega\delta/U_e)^{a_2}}{\left[(\omega\delta/U_e)^{a_3}+a_4\right]^{a_5}+\left[a_6R_T^{a_7}(\omega\delta/U_e)\right]^{a_8}}\ . \tag{4}$$

The Goody model accounts for zero pressure gradient flow and is expressed as a function of the Strouhal number, $\omega\delta/U_e$. This spectrum is calculated using the prescribed parameters $a_1=3, a_2=2, a_3=0.75, a_4=0.5, a_5=3.7, a_6=1.1, a_7=-0.57, a_8=7$.

The Rozenberg et al. (RRM), uses τ_{max} and δ^* as the normalizing parameters replacing τ_w and δ, respectively. The RRM model accounts for the chordwise pressure gradient for flows prior to separation and in this study we assume $\tau_{max}\approx\tau_w$ for cases without flow separation.

$$\frac{\Phi_{pp}U_e}{\tau_{\max}^2\delta^*}=\frac{\left[2.82\Delta^2(6.13\Delta^{-0.75}+F_1)^{A_1}\right]\left[4.2\frac{\Pi}{\Delta}+1\right](\frac{\omega\delta^*}{U_e})^2}{\left[4.76(\frac{\omega\delta^*}{U_e})^{0.75}+F_1\right]^{A_1}+\left[C_3'(\frac{\omega\delta^*}{U_e})\right]^{A_2}}\ . \tag{5}$$

The following parameters are required to calculate Eq. (5):

$$\begin{aligned}&\Delta=\delta/\delta^*, && A_1=3.7+1.5\beta_c, && \Pi=0.8(\beta_C+0.5)^{0.75},\\ &C_3'=8.8R_T^{-0.57}, && A_2=\min\left(3,\tfrac{19}{\sqrt{R_T}}\right)+7, && \beta_c=\tfrac{\theta}{\tau_w}\left(\tfrac{\mathrm{d}P}{\mathrm{dx}}\right),\\ &\text{and } F_1=4.76(1.4/\Delta)^{0.75}\left[0.375A_1-1\right]\end{aligned}$$

The spectrum model by Catlett et al. (CFAS) is also a function of the chordwise pressure gradient $\mathrm{d}P/\mathrm{d}x$. Catlett et al. determined the model parameters of Eq. (4) based on one or more of the following non-dimensional parameters $\beta_\delta=\delta/q_e\cdot\mathrm{d}P/\mathrm{d}x, \beta_\ell=\ell/q_e\cdot\mathrm{d}P/\mathrm{d}x, Re_\ell=U_e\ell/\nu$ and $H=\delta^*/\theta$, where $q_e=0.5\rho U_e^2$ and $\ell=\delta^*\sqrt{C_f/2}$. An important parameter to note is the Clauser parameter β_c, which represents a non-dimensional value of $\mathrm{d}P/\mathrm{d}x$. Other definitions of the Clauser parameter were used in CFAS, β_δ and β_ℓ. Here, β_c is used to indicate the strength of $\mathrm{d}P/\mathrm{d}x$.

For comparison with the measured autospectra, the modeled predictions are normalized using the result from XFOIL. The boundary layer thicknesses and velocity profiles are calculated according to the expression given by Drela[7] as written in Bertagnolio[1] for the DU96-W-180 airfoil.

Finally, Eq. (2) can be used to derive the surface pressure power autospectral density by calculating the single sided integration of $\Phi_{pp}(k_x,k_z,\omega)$ with respect to k_x and k_z.

$$\begin{aligned}\Phi_{pp}(\omega) &= 16\rho^2\int_0^\delta L_y(y)\left[\frac{\partial U}{\partial y}(y)\right]^2\overline{v'v'}(y)\int_0^\infty k_x^2\Phi_m\left[\omega-U_c(y)k_x\right]\\ &\quad \int_0^\infty\frac{\Phi_{vv}(k_x,k_z,y)}{k_x^2+k_z^2}\exp\left[-2\sqrt{k_x^2+k_z^2}\,y\right]\mathrm{d}k_z\,\mathrm{d}k_x\,\mathrm{d}y\end{aligned} \tag{6}$$

In the calculation of Eq. (6) k_x, k_z, and ω are independent variables and to obtain $\Phi_{pp}(\omega)$, k_x and k_z are integrated numerically. The chord-normal velocity autospectrum is modeled with the von Kármán model spectrum for isotropic turbulence

$$\Phi_{vv}=\frac{4}{9\pi k_e^2}\frac{(k_x/k_e)^2+(k_z/k_e)^2}{[1+(k_x/k_e)^2+(k_z/k_e)^2]^{7/3}} \tag{7}$$

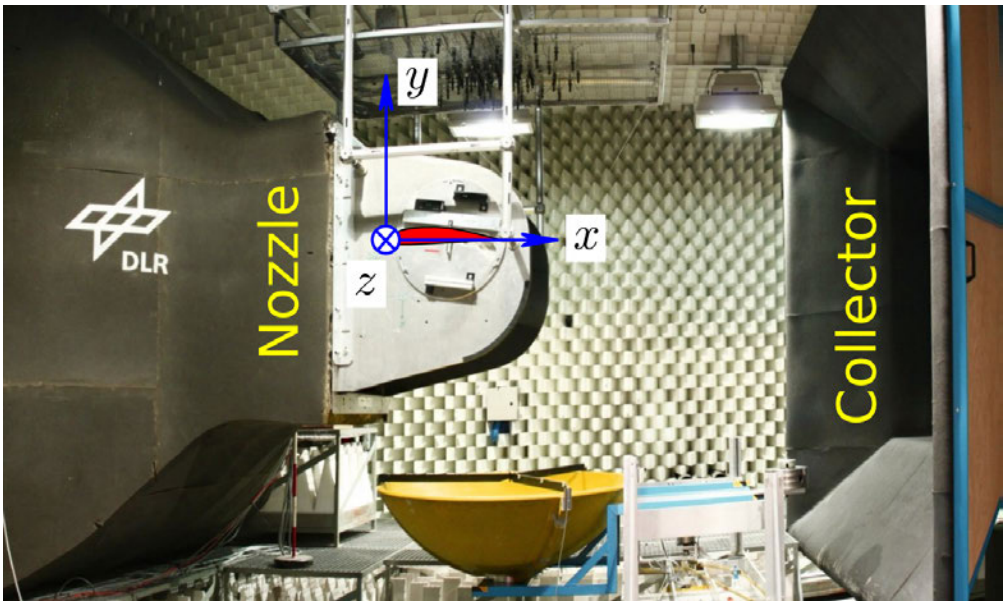

Figure 1. Open test section of the Acoustic Wind Tunnel Braunschweig (AWB). The airfoil and the airfoil relative coordinate system is illustrated.

with $k_e = 0.7468/L_y$ and $L_y = \ell_{mix}/\kappa$, where $\ell_{mix} = 0.085\delta \tanh(\kappa y/0.085\delta)$.[1] The moving axis spectrum is

$$\Phi_m(\omega - U_c(y)k_x) = \frac{1}{\alpha_{\text{Gauss}}\sqrt{\pi}} \exp\left[-\frac{(\omega - U_c(y)k_x)^2}{\alpha_{\text{Gauss}}^2}\right] \tag{8}$$

with $\alpha_{\text{Gauss}} = 0.05U_c(y)/L_y(y)$ and $U_c(y)$ will be defined in Sec. III.F.

II. Experimental setup

Measurements were performed in the anechoic open section of the AWB as shown in figure 1. The wind tunnel's nozzle dimension is 800 mm wide and 1200 mm high with maximum exit velocity of 65 m/s. The turbulence level is 0.3% at the nozzle exit. The airfoil relative coordinate system is given as x chordwise, z spanwise and y chord-normal direction with $x = 0$ at the leading edge and $z = 0$ at the mid-span.

The DU96-W-180 has a span of 800 mm and chord of 300 mm and it is equipped with 62 static pressure taps on both suction and pressure sides. The trailing edge thickness is 0.5 mm. A panel on each side of the model is removable to equip the model with sensors. The panel is 180 mm × 100 mm and when placed on the model the panel adhered to the surface curvature of the model. The wind tunnel model with removable panels is shown in figure 2.

II.A. Surface pressure measurement

Eight piezo-resistive pressure transducers was used with one failing on the last day of the measurement campaign. Major dimensions and the principal setup are documented in figure 3. The mounting of these sensors was designed to be removable, rearrangeable, and can reproduce results easily. To do so, a 12 mm wide channel was milled on the underside of the removable panels and several sensor stations with ⌀=3 mm diameter and 0.5 mm depth were drilled on them. Pinholes of ⌀ =0.5 mm were drilled at the center of these stations. Silicone was molded on the station to fit the sensor's head and create a sealant, while maintaining a clear air passage for the pinhole. To keep the sensors in place mechanical holders in the shape of rods with foam attached on one end were glued on the panels.

The model's lift coefficient were measured in the Laminar Wind Tunnel (LWT) of the Institute of Aerodynamics and Gas Dynamics at the University of Stuttgart and again in the AWB. A zig-zag boundary layer trip (0.205 mm high) was placed at 5% chord from the leading edge on the suction side and another one (0.4 mm high) at 10% chord on the pressure side. The lift coefficient distribution c_l for a range of α and

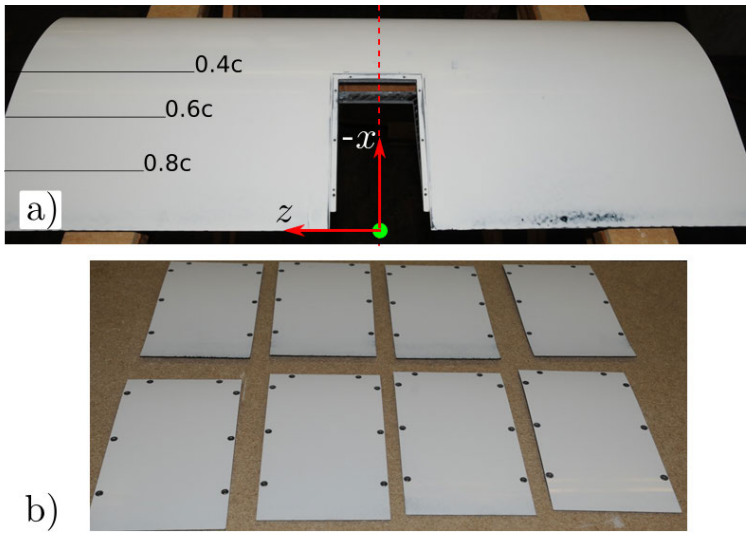

Figure 2. a) DU96-W-180 airfoil, b) 4 sets of removable panels. Surface discoloration near the trailing edge does not influence the surface roughness of the model.

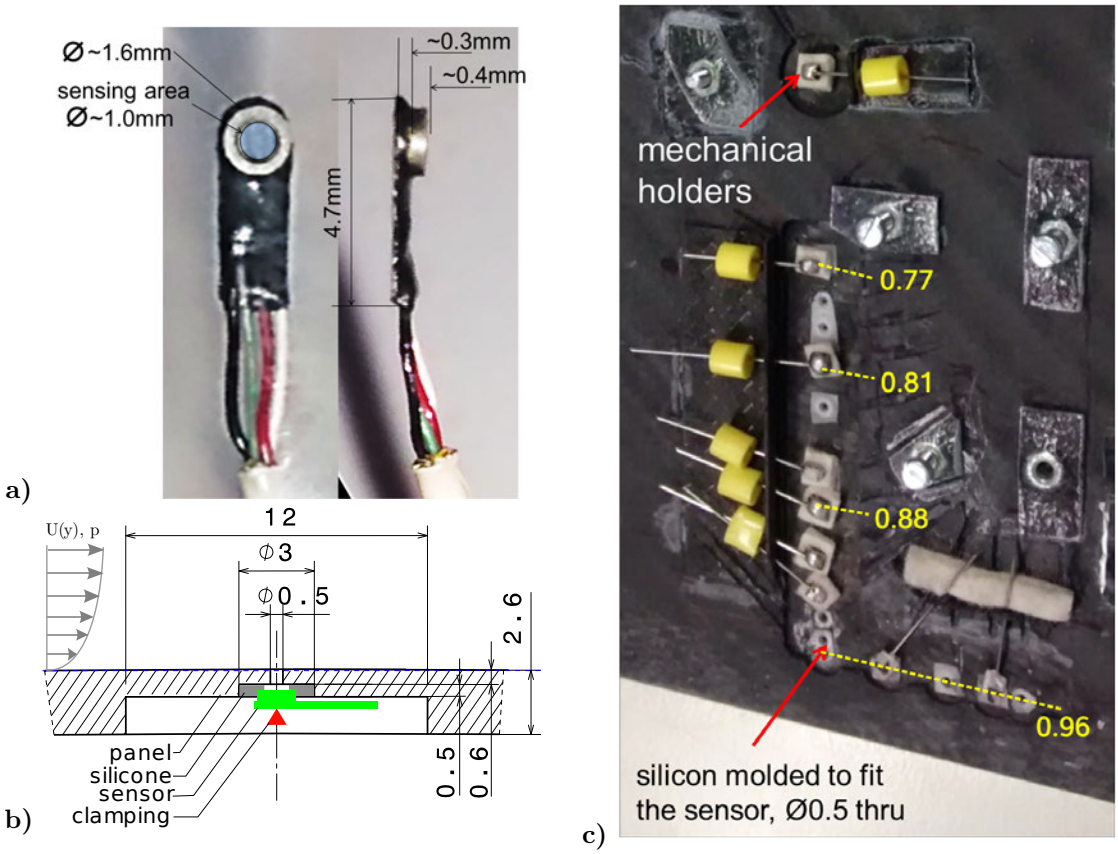

Figure 3. a) Pressure sensor from Kulite semiconductors, b) construction sketch for the installation of the pressure sensor, and c) the underside of one of the removable panels instrumented to accomodate pressure sensors.

chordwise pressure coefficient distribution c_p for $\alpha = 9.4°$ are shown in figure 4. The angle of attack α refers to the aerodynamic angle of attack calculated from XFOIL based on measured lift coefficient as an integral of the static pressure. Figure 4 a) shows good comparison of the polar curve measured in AWB and LWT. Accordingly, a deviation from the linear region of the c_l polar is observed for $\alpha > 4.6°$. This confirms earlier surface ink visualizations, indicating that the boundary layer starts to separate at $\alpha = 4.6°$. The pressure

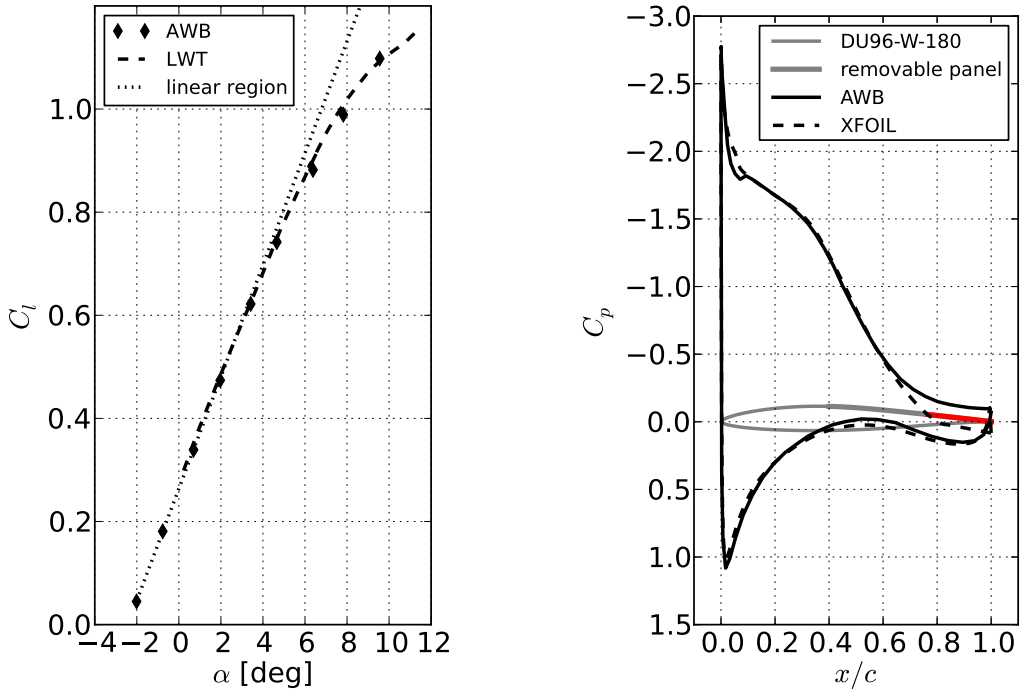

a) b)

Figure 4. a) lift coefficient and b) pressure coefficient at $\alpha = 9.4°$ of the DU96-W-180 airfoil. The airfoil's profile and removable panel are shown as gray colored lines and the range of sensor locations on the suction side is shown in red.

coefficient distributions at $\alpha = 9.4°$ measured in AWB and simulated in XFOIL is shown in figure 4 b) showing good agreement, except for $x/c > 0.6$, where the effect of three-dimensionality from flow separation is strong. Also shown in figure 4 b) is the airfoil's profile and the location of the removable panel in thick gray line. The range of sensor location is shown in red.

An overall number of 8 sensor positions was finally realized with this modular setup. The full measurement matrix included measurements with 5 different sensor arrangements, which were operated at 8 angles of attack $\alpha = (-0.8°, 3.2°, 4.6°, 7.0°, 7.8°, 8.7°, 9.4°,$ and $10.3°)$ and 3 Reynolds numbers $\mathrm{Re} = (0.8, 1.0, 1.2) \times 10^6$. Only surface pressure data for chordwise sensor distributions are shown for $\mathrm{Re} = 1.2 \times 10^6$ to keep this communication brief.

II.B. Velocity measurement

The mean velocity profile at $x/c = 1.01$ was measured using constant temperature anemometry, applying both single-wire and cross-wire probes for the same α and $\mathrm{Re} = 1.2 \times 10^6$.

Computational fluid dynamics (CFD) simulations using the DLR TAU code along with the Reynolds stress turbulence model were additionally performed to evaluate the velocity profiles at the given sensor positions. It was found that the integrated results from CFD simulation is similar to that of XFOIL simulation.

III. Results

III.A. Velocity measurement

The distributions of $U(y; x/c = 1.01)$ are shown in figure 5 for both suction and pressure sides normalized by δ and U_e. These profiles were measured using single wire probes; therefore, figure 5 shows the magnitude of the local velocity. The result of numerical simulations at $x/c = 0.96$ and $x/c = 1.01$ and measurements at $x/c = 1.01$ are compared in figure 6. For $\alpha \leq 4.6°$ the velocity profiles from numerical simulations agree well with the measured profiles, but at $\alpha = 7.0°$ this agreement starts to decline. This is mainly because of the two-dimensionality of the flow is kept in the numerical simulation while in wind tunnel conditions flow separation causes a break in the symmetry of the flow. Based on figure 6, for the prediction of $\Phi_{pp}(\omega)$ using

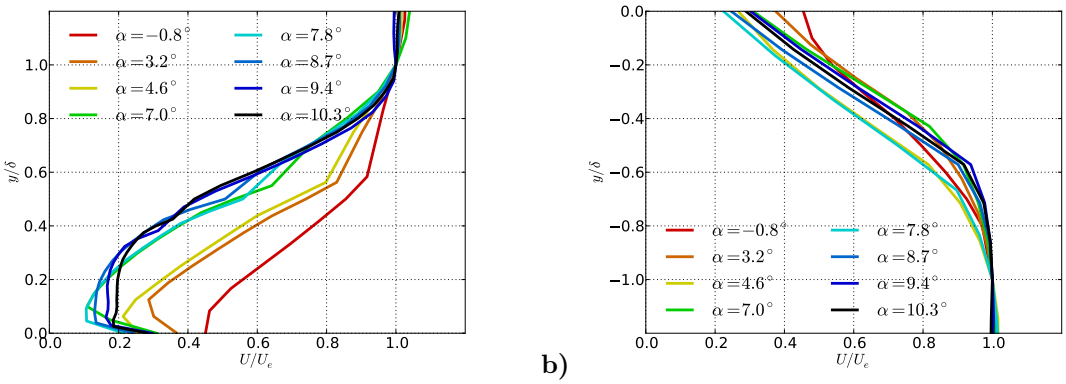

Figure 5. Time averaged velocity measured at x/c= 1.01 for Re = 1.2×10^6 for a) suction side and b) pressure side.

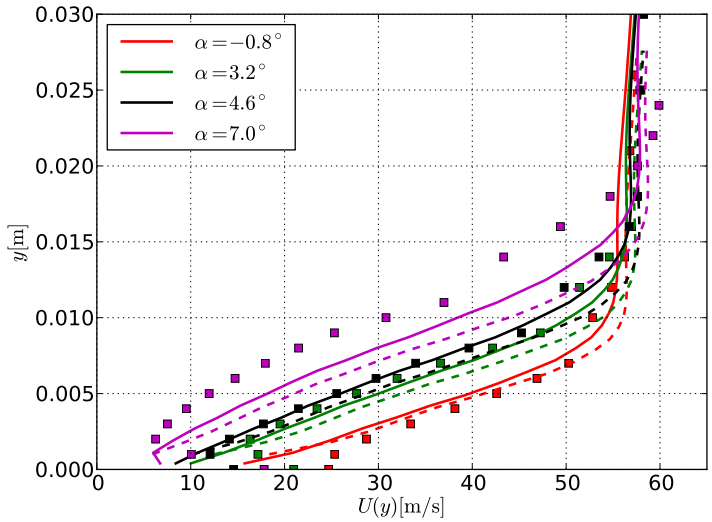

Figure 6. Comparison of velocity profiles from numerical simulation at x/c= 1.01 (——) and x/c= 0.96 (- - -) and measured velocity profiles at x/c= 1.01 (■).

Eq. (6) we assume that the difference between the velocity profile at $x/c = 0.96$ and $x/c = 1.01$ is negligible.

Measured boundary layer properties δ, δ^*, θ, and U_e are listed in table 1 and also listed are the same values at the trailing edge computed with XFOIL. On the suction side the values of $\delta(\alpha \geq 7.8^\circ)$ of the measured and simulated cases diverge by at least 10%, the same can be said about U_e. On the pressure side, XFOIL simulation predicts δ and U_e for $\alpha \leq 7.8^\circ$ well. The prediction of δ^* and θ, however, do not agree with measurement. Because of the limitation in numerical simulations, we consider only the boundary layer properties produced by XFOIL simulation for $\alpha < 7.8^\circ$.

The power autospectral density of the vertical velocity shown in figure 7 are contaminated by high frequency noise that is attributed to electromagnetic interference. Otherwise, the start of the overlap layer and the trend of the spectrum are clear. As critical α is reached and the boundary layer separates from the surface, the eddy in the wake becomes stronger. At $\alpha = 9.4^\circ$ and $\alpha = 10.3^\circ$ a spectral hump can be observed at positions far from the surface with the Strouhal number $\omega c/(2\pi)U_\infty \approx 0.25$. This suggests that the supercritical wake from an attached boundary layer transitions into a turbulent sub-critical wake when the boundary layer separates and transforms an aerodynamically shaped body into an effectively bluff body.

Table 1. Boundary layer properties of the DU96-W-180 measured at x/c= 1.01 and simulated at x/c= 1.00. δ, δ^*, θ are given in mm and U_e is given in m/s.

	Suction side							
	AWB				XFOIL			
$\alpha[\circ]$	δ	δ^*	θ	U_e	δ	δ^*	θ	U_e
-0.8	12	2.61	1.61	54.83	12	4	2	53.14
3.2	16	5.21	2.50	56.97	15	6	2	54.29
4.6	16	5.77	2.55	56.71	16	7	2	55.05
7.0	20	9.37	3.16	57.61	19	10	2	57.32
7.8	22	10.51	3.39	59.63	20	12	2	58.15
8.7	26	12.86	3.91	63.38	22	14	2	59.08
9.4	34	16.40	5.09	64.94	24	16	2	59.77
10.3	40	19.39	6.32	66.71	27	19	3	60.71
	Pressure side							
	AWB				XFOIL			
$\alpha[\circ]$	δ	δ^*	θ	U_e	δ	δ^*	θ	U_e
-0.8	10	2.37	1.45	54.35	9	2.1	1.3	53.14
3.2	8	1.77	1.05	56	7	1.4	0.9	54.29
4.6	7	2.16	1.08	54.62	7	1.2	0.8	55.05
7.0	7	1.56	0.86	57.76	6	0.9	0.6	57.32
7.8	6	1.88	0.9	57.31	5	0.8	0.6	58.15
8.7	7	1.84	0.91	62.44	5	0.8	0.5	59.08
9.4	7	1.59	0.85	63.66	5	0.7	0.5	59.77
10.3	7	1.7	0.88	65.39	4	0.7	0.5	60.71

III.B. Pressure spectra of the turbulent boundary layer with non zero pressure gradient

Figure 8 shows Φ_{pp} for the position closest to the trailing edge $x/c = 0.96$ from 3 independent measurements. The spectra fit each other very well showing that the installation of the sensors can produce repeatable results. The maximum of Φ_{pp} increases proportionally with α and the peak frequency shifts to the lower frequencies. An increase of approximately 15 dB is shown in figure 8 between $\alpha = -0.8^\circ$ and $\alpha = 10.3^\circ$. The roll-off starts earlier and the spectrum decays more rapidly with increasing α.

Tables 2 and 3 list the Rotta-Clauser parameter β_c that is the non-dimensional representation of the pressure gradient. These parameters are calculated using both measurement data ($\mathrm{d}P/\mathrm{d}x$) and XFOIL simulation (θ and τ_w). Only β_c values where the boundary layer remains attached, i.e. has a finite τ_w, are listed.

Figure 9 shows $\Phi_{pp}(\omega, x/c)$ for each α. With higher α and stronger adverse pressure gradient, the spectral decay becomes more rapid and starts earlier. Particularly, a frequency shift towards lower frequencies with growing $\delta(x/c)$ is observable. For $-0.8^\circ \leq \alpha \leq 4.6^\circ$ $\Phi_{pp}(\omega, x/c)$ is distinct. This distinction becomes less clear with higher α and with positions x/c sufficiently close to the trailing edge. For example, at $\alpha = 10.3^\circ$ $\Phi_{pp}(\omega, x/c)$ collapse to almost a single spectrum. Figure 9 suggests that for separated turbulent boundary layers the pressure spectra can be treated as a homogeneous flow in the chordwise direction.

The pressure spectra $\Phi_{pp}(\omega, x/c)$ on the pressure side as shown in figure 10 shows a flattening of the spectra for the high frequency region as an effect of favorable pressure gradient. Two sensors at $x/c = 0.88$ and 0.81 show a discrepancy in the low frequency region, which suggest that they were misaligned during the measurement. A single peak in the spectra is shown to develop with increasing α and with downstream chordwise positions. This peak appears at the same frequencies as the respective spectral maxima in the suction side Φ_{pp}. The characteristics of the pressure fluctuation spectra can be better understood after non-dimensionalization of Φ_{pp} using boundary layer values.

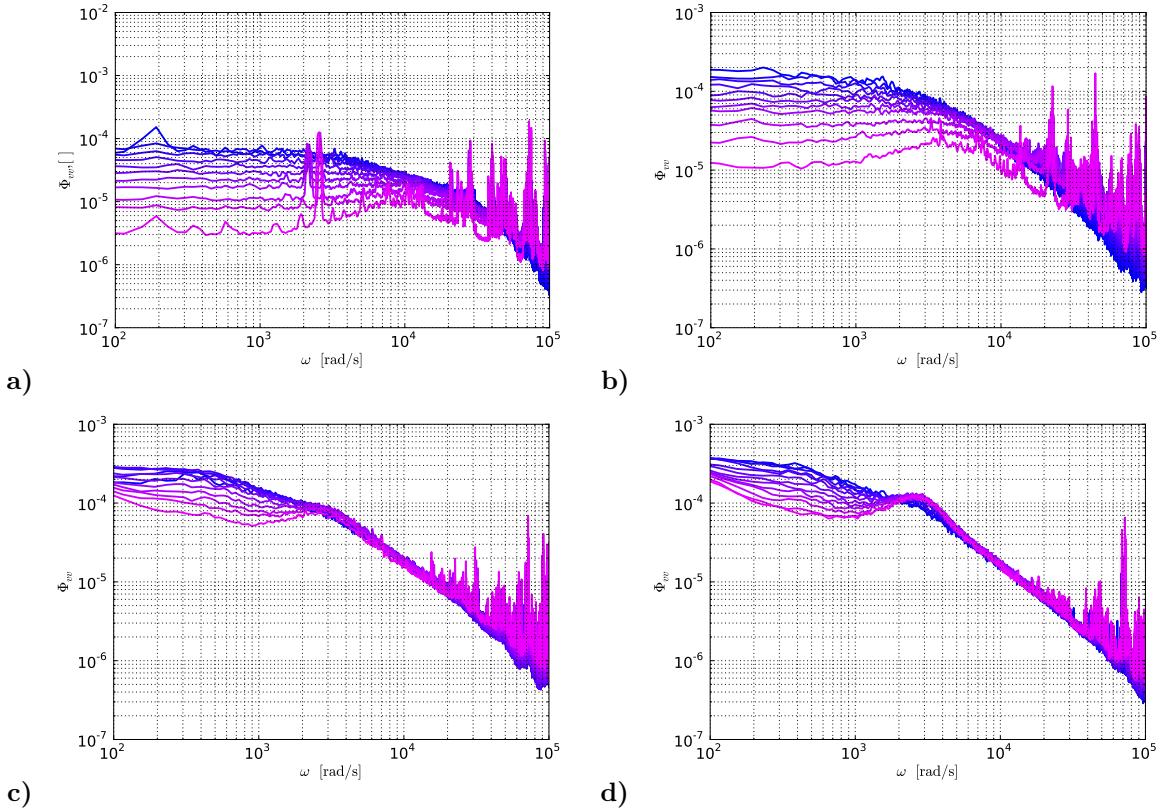

Figure 7. Vertical velocity autospectrum for a) $\alpha = -0.8^\circ$, b) $\alpha = 7.0^\circ$, c) $\alpha = 9.4^\circ$, d) $\alpha = 10.3^\circ$ where the line color from blue to magenta represents positions at increasing height from the surface.

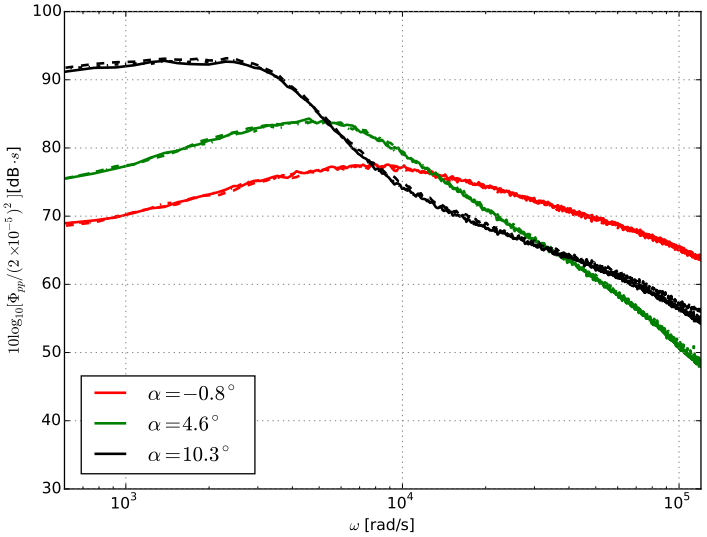

Figure 8. Autospectra near the trailing edge $x/c = 0.96$ from three independent measurements.

III.C. Pressure spectra normalized with τ_w and δ^*/U_e

Based on the boundary layer properties from XFOIL, the local τ_w, δ^*, and U_e are used to normalize the measured pressure spectra as shown in figure 11 for the suction side and in figure 12 for the pressure side. Because of discrepancies induced by the effects of separation at high α between measured and XFOIL values, only $\Phi_{pp}(\alpha \leq 7.8^\circ)$ are considered. On the suction side only $\Phi_{pp}(\alpha \leq 4.6^\circ)$ are shown, because for $\alpha > 4.6^\circ$,

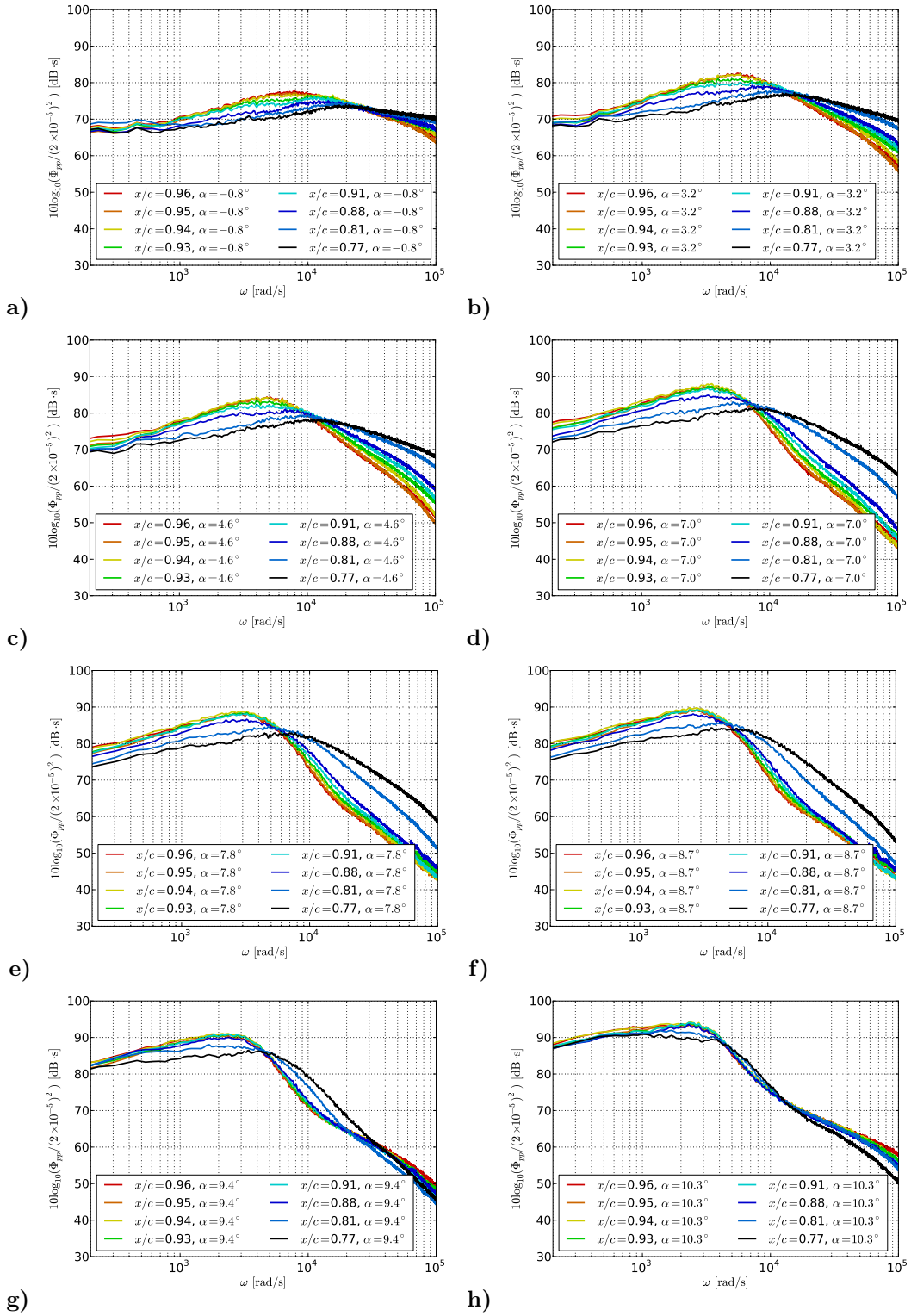

Figure 9. Suction side $\Phi_{pp}(\omega)$ for the 8 selected α.

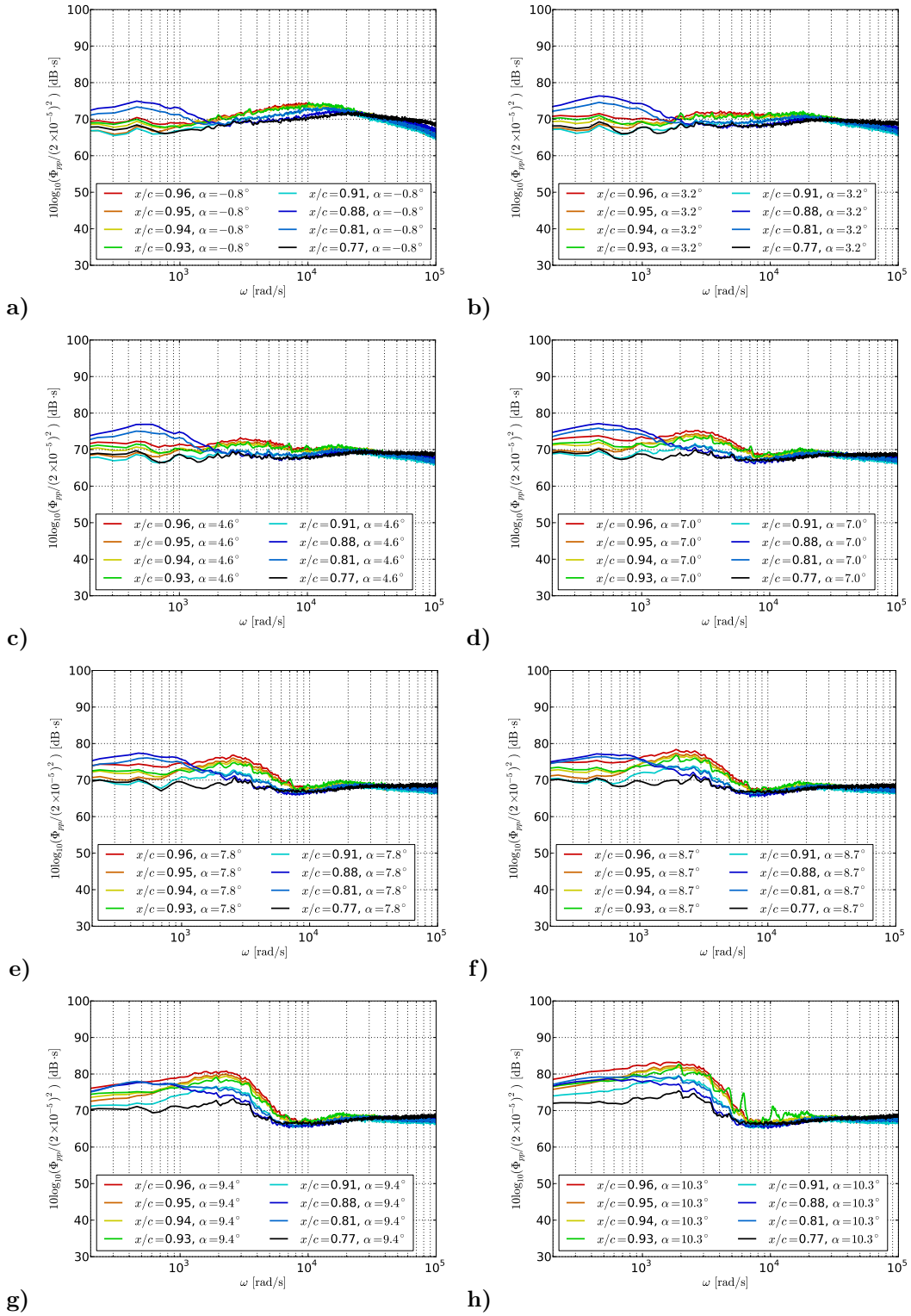

Figure 10. Pressure side $\Phi_{pp}(\omega)$ for the 8 selected α.

Table 2. Non-dimensional pressure gradient β_c on the suction side.

$\alpha[^\circ]$	x/c							
	0.96	0.95	0.94	0.93	0.91	0.88	0.81	0.77
−0.8	7.06	6.27	5.33	4.33	3.17	2.33	1.34	0.99
3.2	14.03	12.56	10.77	8.82	6.50	4.83	2.62	1.84
4.6	17.44	18.80	13.73	11.42	8.60	6.58	3.42	2.38
7.0	169.69	98.25	50.81	31.42	19.36	13.87	6.25	4.12
7.8		14160.21	973.18	331.048	55.35	21.53	8.13	5.20

Table 3. Non-dimensional pressure gradient β_c on the pressure side.

$\alpha[^\circ]$	x/c							
	0.96	0.95	0.94	0.93	0.91	0.88	0.81	0.77
−0.8	0.54	0.84	1.25	1.74	2.03	1.92	1.69	1.34
3.2	−0.52	−0.24	0.11	0.56	0.91	0.95	1.01	0.85
4.6	−0.75	−0.50	−0.19	0.23	0.58	0.67	0.84	0.71
7.0	−0.44	−0.35	−0.24	−0.06	0.13	0.22	0.40	0.41
7.8	−0.45	−0.37	−0.27	−0.12	0.06	0.19	0.36	0.39
8.7	−0.58	−0.49	−0.37	−0.17	0.04	0.13	0.30	0.31
9.4	−0.50	−0.43	−0.36	−0.23	−0.08	0.06	0.24	0.28
10.2	−0.52	−0.45	−0.38	−0.25	−0.10	0.02	0.21	0.24

$\tau_w \to 0$ in the vicinity of the trailing edge. While the measured and simulated δ^* on the pressure side do not agree, the values from XFOIL simulation are used because the measured data is an integration over a thin boundary layer. The number of discrete positions is smaller for thinner boundary layers.

As expected the pressure spectra in figure 11 do not collapse with the given normalizing parameters. Due to adverse pressure gradient the maximum of $\Phi_{pp}(\omega, x/c)$ increases with increasing α. In figure 12 the normalization parameters collapse the pressure side Φ_{pp} for $\alpha = 7.0^\circ$ and $\alpha = 7.8^\circ$. In the low frequency region, $\Phi_{pp}(\omega\delta^*/U_e < 0.2)$ has a peak and a valley before reaching a plateau. These contributions cannot be explained by the pressure side boundary layer but seem to be an effect of the scattering of the suction side hydrodynamic pressure field (viz. trailing edge noise in its acoustical near-field). As observable in figures 9 and 10 these scattered contributions are about 10 dB below the Φ_{pp} levels measured on the suction side. Note that the corresponding scattered contributions originating from the pressure side are not observable in the suction side Φ_{pp} (i.e. the sensors appear to be far enough from the trailing edge, given the smaller hydrodynamical wavelengths of the typical eddies at the pressure side).

III.D. Pressure spectra normalized with q_e and δ/U_e

Another way to normalize Φ_{pp} is using the local dynamic pressure q_e as shown in figures 13 and 14. The overlap collapses well with q_e for moderate adverse pressure gradients. The maximum of the normalized suction side Φ_{pp} is $-36\text{dB} \pm 1\text{dB}$ for $\alpha \geq 7.0^\circ$ in the vicinity of the trailing edge.

The peak of the pressure side Φ_{pp} do not collapse with the normalizing parameters in agreement with the argument in the previous section that the pressure side Φ_{pp} is affected by the scattering of the suction side hydrodynamic pressure field.

III.E. Evaluation of empirical models of surface pressure power spectrum density

Figure 15 shows Φ_{pp} for $\alpha = -0.8^\circ$ and 4.6°. Both figures show $x/c = 0.96, 0.88, 0.77$ from top to bottom. In these figures, the absolute levels of the Goody model are increased by 3.5 dB and by 7.5 dB for the CFAS model. These increments were selected based on arbitrary fitting of the model spectrum to the measured

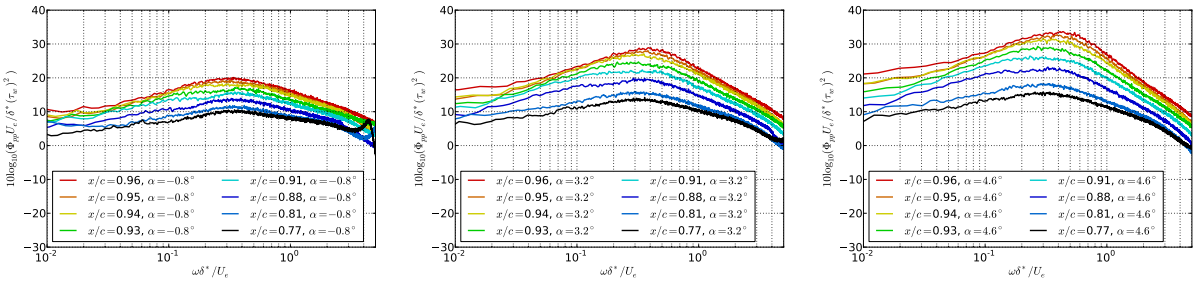

Figure 11. Pressure spectra on the suction side normalized by τ_w and δ^*/Ue for $\alpha = -0.8°, 3.2°, 4.6°$

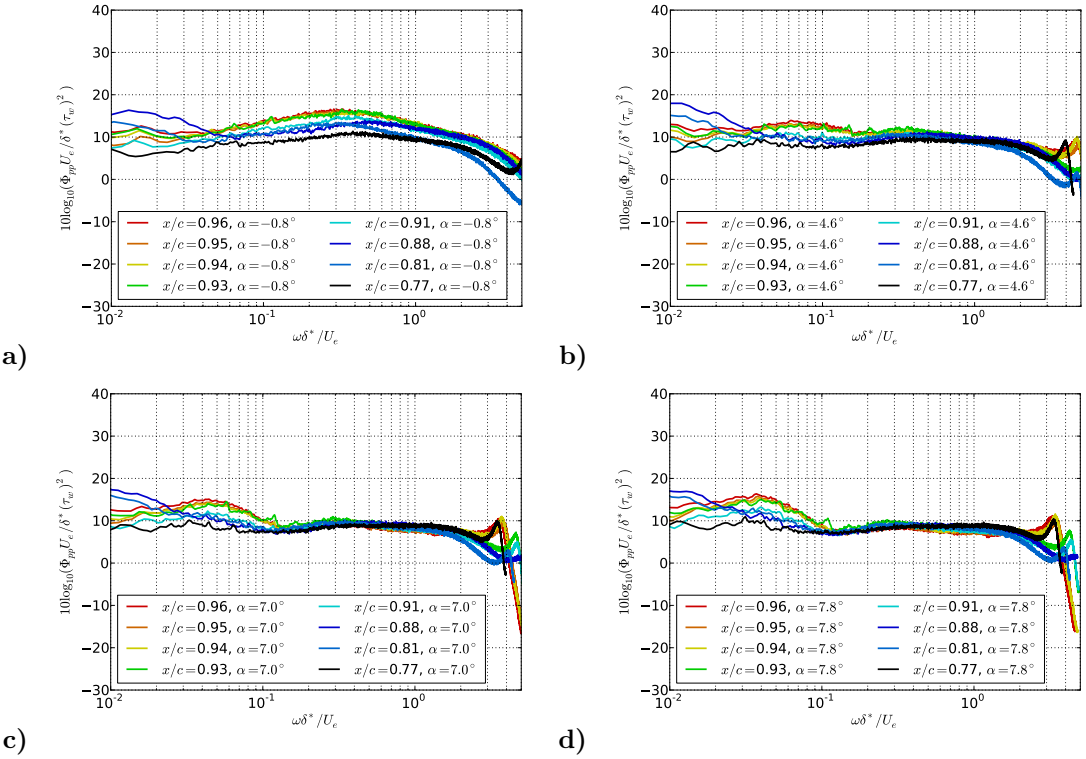

Figure 12. Pressure spectra on the pressure side normalized by τ_w and δ^*/Ue for a) $\alpha = -0.8°$, b) $4.6°$, c) $7.0°$, and d) $7.8°$.

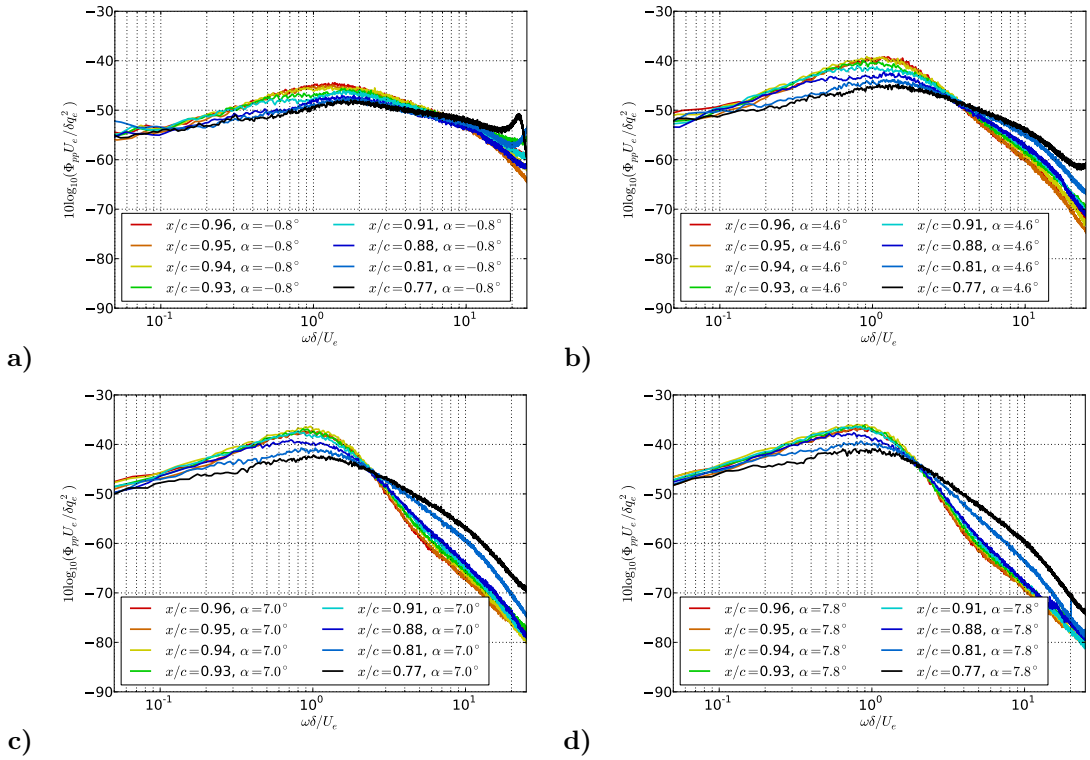

Figure 13. Φ_{pp} **on the suction side normalized by** q_e **and** δ/Ue **for a)** $\alpha = -0.8°$**, b) 4.6°, c) 7.0°, and d) 7.8°.**

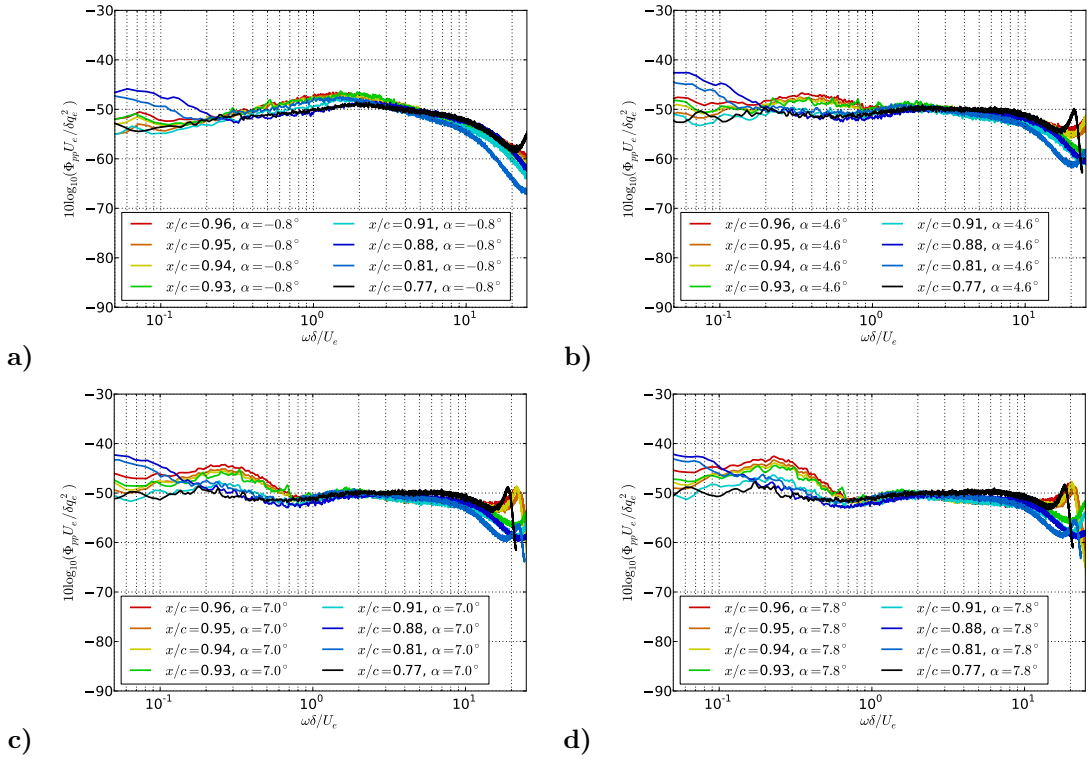

Figure 14. Φ_{pp} **on the pressure side normalized by** q_e **and** δ/Ue **for a)** $\alpha = -0.8°$**, b) 4.6°, c) 7.0°, and d) 7.8°..**

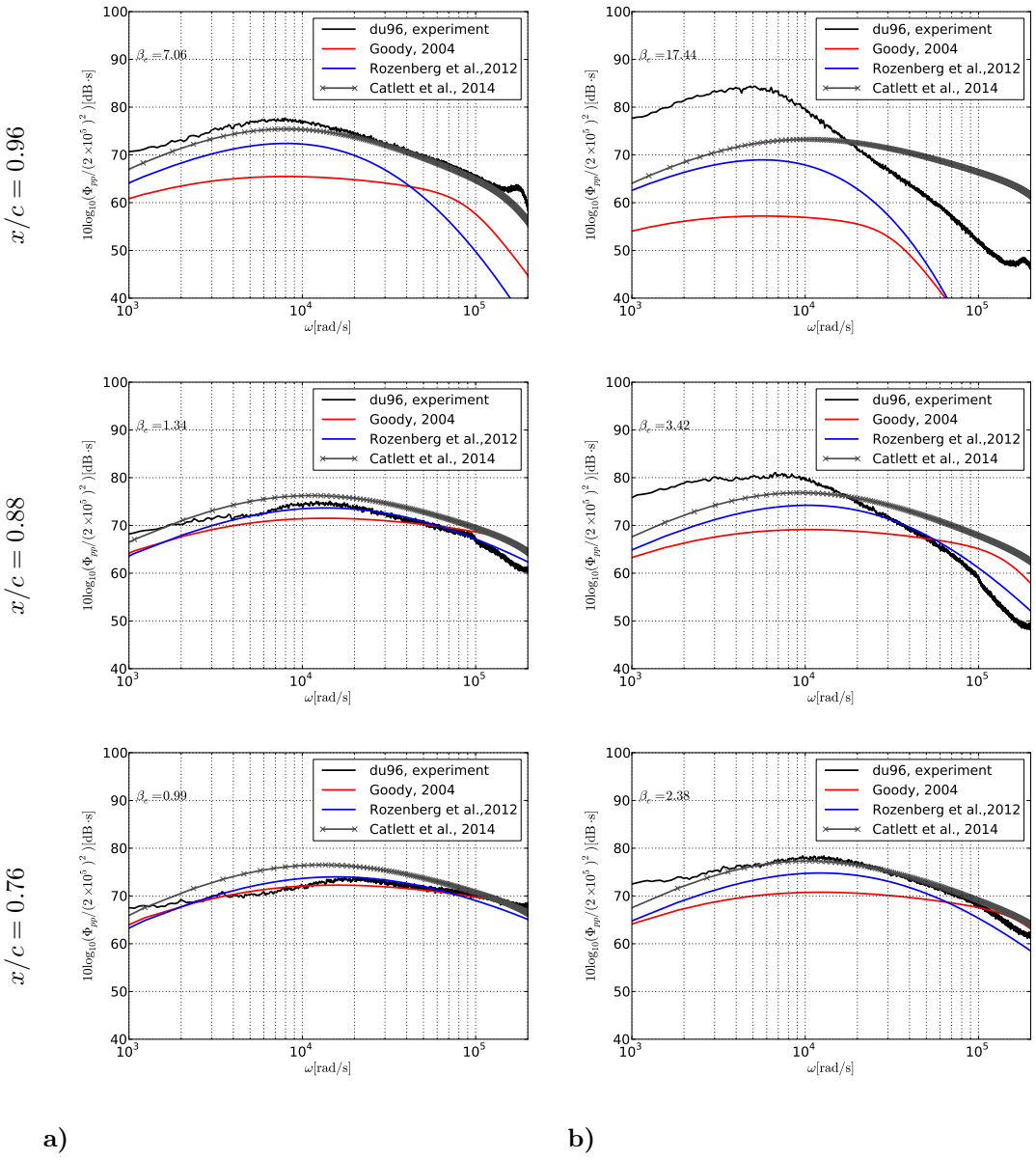

Figure 15. Surface pressure spectra on the suction side along the chordwise positions from top to bottom x/c= 0.96, 0.88, 0.76 mm for a) α= −0.8° and b) α= 4.6°.

spectrum. In figure 15 a) $\Phi_{pp}(f; x = 0.96)$ behaves according to the CFAS model but deviation starts as β_c decreases and $\Phi_{pp}(\omega; x/c = 0.77)$ follows the spectral shape given by the Goody model. Here, the difference of power level from the zero pressure gradient spectrum of Goody can be attributed to the pressure gradient. A similar increase can also be observed in Ref. 12. For all configurations, the RRM model fails to predict the transition location from the overlap to high frequency region. Issues with the RRM model were discussed in Ref. 5. In figure 15 b), similar trends to the previous figure can also be observed; Φ_{pp} is influenced by the increase of β_c. However, at $x/c \geq 0.88$ the CFAS spectra fail to capture the spectral trend because at $\alpha = 4.6°$ the boundary layer near the trailing edge has separated.

III.F. Prediction of surface pressure power spectrum density with modified Blake-TNO model

The pressure autospectral density was predicted using Eq. 6. In this study and also in Ref. 14, a discussion about the convective velocity is focused whether $U_c(y) = 0.7U(y)^{10}$ or $U_c(y) = U(y)$. The reason for the latter ratio is that the turbulent eddy is expected to travel with the local velocity. To establish the proper

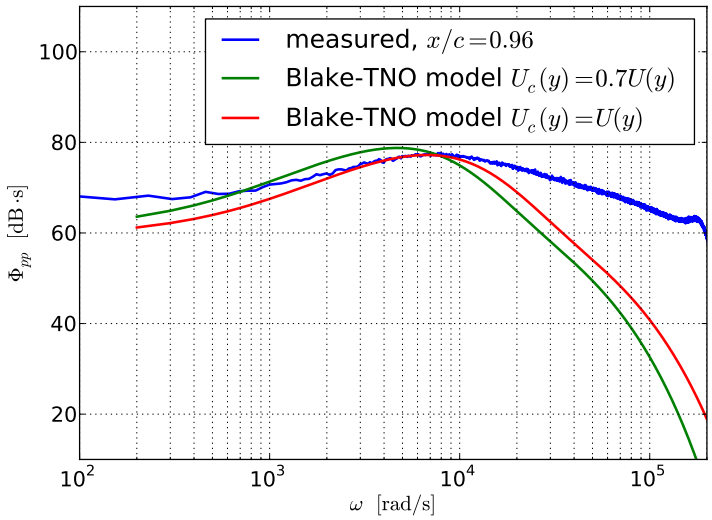

Figure 16. Pressure autospectra for the trailing edge position for $\alpha = -0.8°$.

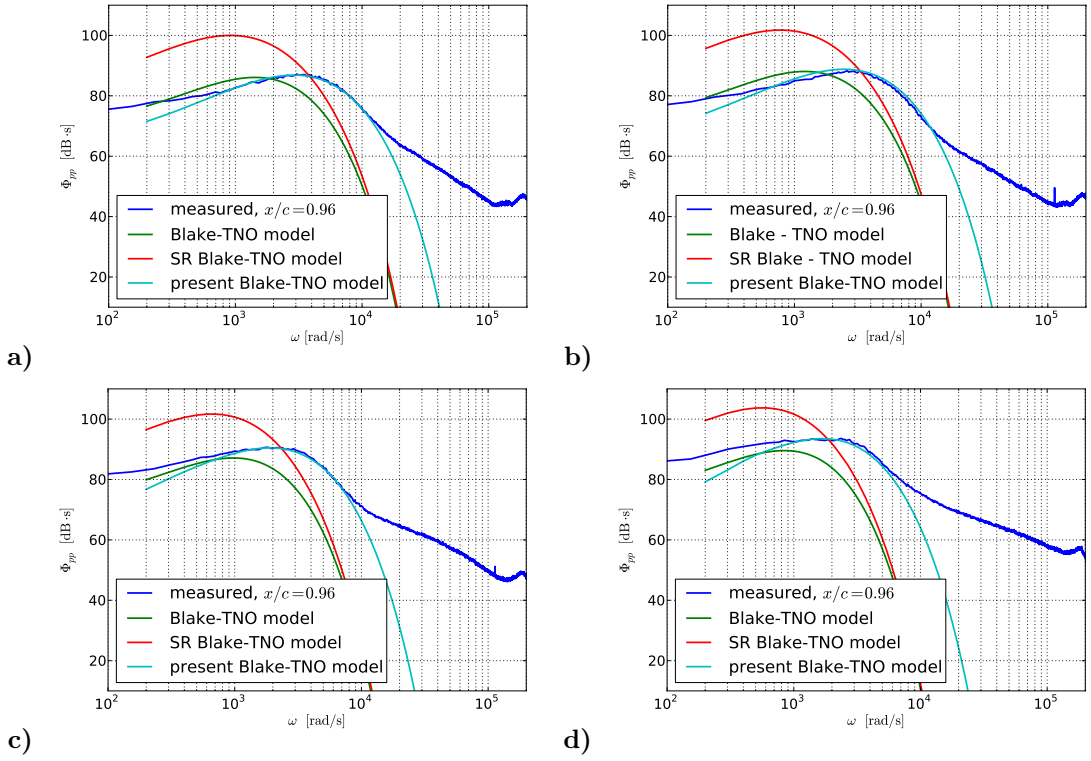

Figure 17. Surface pressure autospectra at x/c= 0.96 for a) α= 7.0°, b) α= 7.8°, c) α= 8.7°, and d) α= 10.3°.

relationship, $\Phi_{pp}(\omega;\alpha = -0.8°)$ was calculated and it was found that $U_c(y) = U(y)$ provided the correct levels as shown in Fig. 16. In the integration of Eq. (6) the measured chord-normal distributions $0 \leq y \leq \delta$ of $\mathrm{d}U/\mathrm{d}y$ and $\overline{v'v'}$ were used.

Figure 17 shows $\Phi_{pp}(\omega; 7.0° \leq \alpha \leq 10.3°)$. Here, the integration with respect to y was defined from a certain height from the surface to the edge of the boundary layer because of the presence of reversed flow. This range is listed in table 4. The modifications of U_c and L_y as proposed in Ref. 14 (SR, $U_c(y) = 0.7U(y), L_y = 2.5\ell_{mix}/\kappa$) over-predict the magnitude of the power spectrum and provide a roll off that starts too early. The original Blake-TNO model ($U_c(y) = 0.7U(y), L_y = \ell_{mix}/\kappa$) is shown as the green line

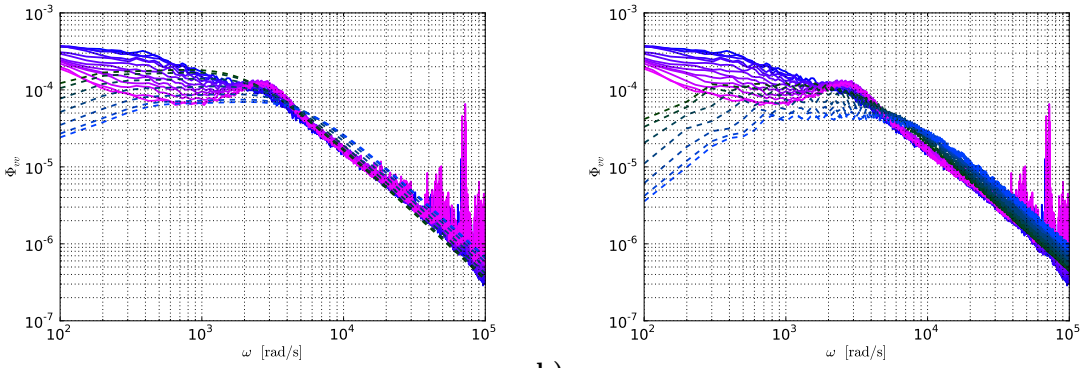

a) **b)**

Figure 18. Vertical velocity spectrum, $\Phi_{vv}(\omega)$ at $\alpha = 10.3^\circ$ a) Original Blake-TNO model and b) present Blake-TNO model with $c_1 = 1.3, c_2 = 1.6$.

in figure 17 and it under-predicts the power spectrum. The present prediction was done by modifying the moving axis spectrum .

$$\Phi_m(\omega - c_1 U_c(y) k_x) = \frac{1}{\alpha_{\text{Gauss}}\sqrt{\pi}} \exp\left[-\frac{(\omega - c_1 U_c(y) k_x)^2}{\alpha_{\text{Gauss}}^2}\right] \tag{9}$$

and $L_y = c_2 \ell_{mix}/\kappa$, where c_1 and c_2 are determined heuristically and given in Table 4. These modifications

Table 4. y Range of integration in y and moving axis modifier c_1, c_2.

α	y[mm]	c_1	c_2
7.0°	$7 \leq y \leq 20$	1.3	1.6
7.8°	$8 \leq y \leq 24$	1.3	1.6
9.4°	$8 \leq y \leq 30$	1.5	1.6
10.3°	$16 \leq y \leq 40$	1.6	1.7

are analogous to a change in the correlation length scales L_x, L_y for a separated boundary layer. The chordwise length scale L_x decreases and the chord normal length scale L_y increases for $\alpha \geq 7.0^\circ$. The smaller value of L_x can be directly attributed to the increase rate of dissipation as seen in the measured $\Phi_{pp}(\omega)$.

The vertical velocity spectrum was modeled using the von Kármán isotropic spectrum model and shown as dashed line in figure 18. This spectral curve is an integration of

$$\Phi_{vv}(\omega; y) = \int_0^\infty \int_0^\infty \Phi_{pp}(k_x, k_z) \Phi_m(\omega - c_1 U_c(y) k_x)\, \mathrm{d}k_x \mathrm{d}k_z \tag{10}$$

The dashed line color varies from black to blue indicating positions of increasing distance from the surface. The isotropic model under-predicts the measured spectra significantly, in particular at positions far from the surface it does not represent the spectral hump as shown in figure 18. With the proposed modifications the prediction of Φ_{vv} is worse. However, increasing the integrand L_y in Eq. (6) with a factor of c_2 compensates for the magnitudes of Φ_{vv}.

IV. Conclusions

The goal of this project is to develop a model for the prediction of far-field trailing edge noise induced by a separated turbulent boundary layer. In part of this, a DU-96-W-180 airfoil was equipped with miniature surface pressure sensors to measure the local surface pressure fluctuations. In this communication the measured surface pressure autospectral density is compared with that given by empirical and semi-empirical models.

The mean velocity profile was measured at 1%c behind the trailing edge. The velocity profile was compared with CFD simulation results, where for sufficiently two-dimensional flow (i.e. $\alpha \leq 7.0^\circ$) the velocity

profiles agree reasonably. The boundary layer properties were evaluated by XFOIL simulation, where also for sufficiently two-dimensional flows (i.e. $\alpha \leq 7.8°$) the boundary layer properties agree well.

Flow separation affects the suction side surface pressure spectra as an increase of power level in the low frequency region. Downstream of the point of separation of the turbulent boundary layer, the surface pressure spectrum is independent of the chordwise positions. This suggests that the turbulent boundary layer inside the separation region can be approximated as a chordwise homogeneous flow. On the pressure side favorable pressure gradient condition is met, which in effect flattens the surface pressure spectra at the high frequency range. Near-field trailing edge noise contributions can be observed on the pressure side at frequencies that correspond to the suction side hydrodynamical pressure spectral peaks, due to the hydrodynamical pressure on the pressure side is dominated by smaller wavelengths with lower levels compared to the suction side hydrodynamic pressure field.

The SR modifications of the correlation length scale and convective velocity are found to produce incorrect levels and earlier spectral roll off. A modification to the moving axis spectra is proposed to fit the measured surface pressure power spectral density. A physical analogy is proposed that the modifying parameters shortened the chordwise correlation length scale and lengthened the chord-normal one. Measured data for the chord-normal correlation length scale are currently under evaluation to validate the present modifications of the Blake-TNO model and the frequency-wavenumber spectra are to be analyzed for the prediction of the far-field noise.

Acknowledgments

This work was sponsored by GE Wind Energy, GmbH, Salzbergen, Germany.

References

[1]Bertagnolio, F., *Trailing edge noise model applied to wind turbine airfoils, Risø-R-1633(EN)*, RisøNational Laboratory, Technical University of Denmark, Denmark, 2008.

[2]Blake, W.K., *Mechanics of Flow-Induced Sound and Vibration*, Academic Press, London, 1986.

[3]Brooks, T.F., and Hodgson, T.H., *Trailing edge noise prediction from measured surface pressures*, Journal of Sound and Vibration, vol. 78, no. 1, 1981.

[4]Brooks, T.F., Pope, D.S., and Marcolini, M.A., *Airfoil self-noise and prediction*, NASA Reference Publication 1218, 1989.

[5]Catlett, M.R., Forest, J.B., Anderson, J.M., and Stewart, D.O., *Empirical spectral model of surface pressure fluctuations beneath adverse pressure gradients*, Proceedings of the 20$^{\text{th}}$ AIAA/CEAS Aeroacoustic Conference, Atlanta, GA, AIAA paper 2014-2910, 2014.

[6]Corcos, G.M., *The structure of the turbulent pressure field in boundary-layer flows*, Journal of Fluid Mechanics, vol. 18, no. 3, 1964.

[7]Drela, M., *XFOIL: An analysis and design system for low Reynolds number airfoils*, in Low Reynolds number aerodynamics, Mueller, T.J. (ed), Lecture Notes in Engineering, vol. 54, Springer-Verlag, Berlin 1989.

[8]Goody, M., *Empirical spectral model of surface pressure fluctuations*, AIAA Journal, vol. 42, no. 9, 2004.

[9]Howe, M.S., *Trailing edge noise at low Mach numbers, part 2: Attached and separated edge flows*, Journal of Sound Vibration, vol. 234, no. 5, 2000.

[10]Parchen, R., *Progress report DRAW: A prediction scheme for trailing-edge noise based on detailed boundary-layer characteristics*, TNO report HAG-RPT-980023, TNO Institute of Applied Sciences, The Netherlands, 1998.

[11]Rozenberg, Y., Gilles, R., and Moreau, S., *Wall-pressure spectral model including the adverse pressure gradient effects*, AIAA Journal, vol. 50, no. 10, 2012.

[12]Schloemer, H.H.: *Effects of pressure gradient on turbulent-boundary-layer surface-pressure fluctuations*, The Journal of the Acoustical Society of America, vol. 42, no. 1, 1967

[13]Schüle C.Y., *First milestone meeting: Flow separation study*, DLR Internal report, 2012

[14]Schüle, C.Y., and Rossignol, K.S., *Trailing edge noise modeling and validation for separated flow conditions*, Proceedings of the 19$^{\text{th}}$ AIAA/CEAS Aeroacoustic conference, Berlin, Germany, AIAA paper 2013-2008, 2013.